

Twisted Trilayer Graphene, Quasiperiodic Superconductor

Xinghai Zhang,¹ Ziyang Zhu,² Justin H. Wilson,^{3,4} and Matthew S. Foster^{1,5}

¹*Department of Physics and Astronomy, Rice University, Houston, Texas 77005, USA*

²*Department of Physics, Boston College, 140 Commonwealth Avenue Chestnut Hill, MA 02467, USA*

³*Department of Physics and Astronomy, Louisiana State University, Baton Rouge, LA 70803, USA*

⁴*Center for Computation and Technology, Louisiana State University, Baton Rouge, LA 70803, USA*

⁵*Rice Center for Quantum Materials, Rice University, Houston, Texas 77005, USA*

(Dated: December 30, 2025)

Twisted multilayer moiré materials are generically quasiperiodic on the moiré scale due to the interference of different misaligned moiré periodicities. Spatial inhomogeneities such as these can be detrimental to superconductivity [1, 2]; nonetheless, superconductivity has been observed in quasiperiodic twisted trilayer graphene (TTG) [3]. Here, we systematically study the superconducting properties of TTG. We reveal that an interplay between quasiperiodicity and topology drives TTG into a critical regime, enabling it to host superconductivity with rigid phase stiffness for a wide range of twist angles, rather than at a fine-tuned value. The criticality in the normal state is due to the Dirac fermions coupled by quasiperiodic tunneling *simulating* 3D topological superconductor surface states [4]. This critical-metal regime is marked by multifractal wave functions across the spectrum and scale-invariant transport reminiscent of the integer quantum Hall plateau transition. We demonstrate this with large-scale wave function and Kubo conductivity calculations. These observations lead to a clear experimental implication: stronger interlayer coupling in TTG further stabilizes both the criticality and superconductivity, allowing superconductivity to be seen across a wider range of angles with experimentally accessible pressures.

Twisted multilayer graphene has recently emerged as a powerful platform for exploring strongly correlated electronic phases. Interference between multiple moiré patterns generates additional long-wavelength scales beyond those in bilayer systems. The secondary moiré-of-moiré scale [5] can be substantially larger than individual moiré patterns even when slightly misaligned, and it is generically quasiperiodic (incommensurate) in the continuum limit. This additional structural degree of freedom leads to a variety of electronic behaviors [6–9] and creates a landscape distinct from that of the bilayer case [10–14]. Nonetheless, recent experiments on twisted trilayer graphene (TTG) reveal superconductivity [3, 6, 15–17], anomalous Hall responses [16, 18], and correlated insulating states [15, 17, 19]. These observations suggest TTG is not a simple perturbation of TBG, but a distinct platform for new correlated phases.

Quasiperiodicity in low dimensions is usually expected to suppress transport by driving electronic states towards Anderson localization [20]. This raises a fundamental question: how can robust superconductivity appear in a system whose underlying single-particle electronic wave functions are, naively, strongly inhomogeneous or even localized? In ordinary two-dimensional (2D) systems, increasing spatial inhomogeneity predominantly suppresses phase coherence and reduces the superfluid stiffness, often destroying superconductivity, rather than promoting it [2, 21, 22].

The key is that graphene-based moiré materials differ from conventional 2D systems. Their low-energy Dirac fermions are coupled between layers by effective long-wavelength non-Abelian gauge potentials. This places TTG in a class analogous to topological surface states, where topology can protect the system from Anderson localization and stabilize critical transport even in the presence of strong inhomogeneity [4, 23, 24]. As a result, quasiperiodic TTG can enter a metallic regime in which *all* wave functions across a broad energy window become quantum critical (“multifractal” [25]) and transport acquires a scale-invariant character reminiscent of the integer quantum Hall plateau transition [23]. This “critical metal” is neither ballistic nor localized: with conductivity $\sim e^2/h$ over a wide range of energies. Such critical wave functions are known to enhance pairing [1, 4, 22, 26, 27], providing a mechanism by which quasiperiodicity can stabilize robust superconductivity in TTG.

Here we demonstrate quasiperiodicity-enhanced superconductivity in TTG. Using large-scale continuum-model simulations, we show that generic incommensurate twist-angle pairs yield a superconducting phase with sizable superfluid stiffness across a broad range of angles. We attribute this behavior to the presence of quantum-critical electronic states in the normal phase, as seen in multifractal wave function diagnostics and Kubo conductivity. We further show that increasing the interlayer coupling—achievable via hydrostatic pressure [33–35]—stabilizes the criticality and strengthens superconductivity. Together, these results establish TTG as a platform where quasiperiodicity and electronic topology conspire to stabilize superconductivity beyond a narrow, fine-tuned flat-band (magic-angle) regime.

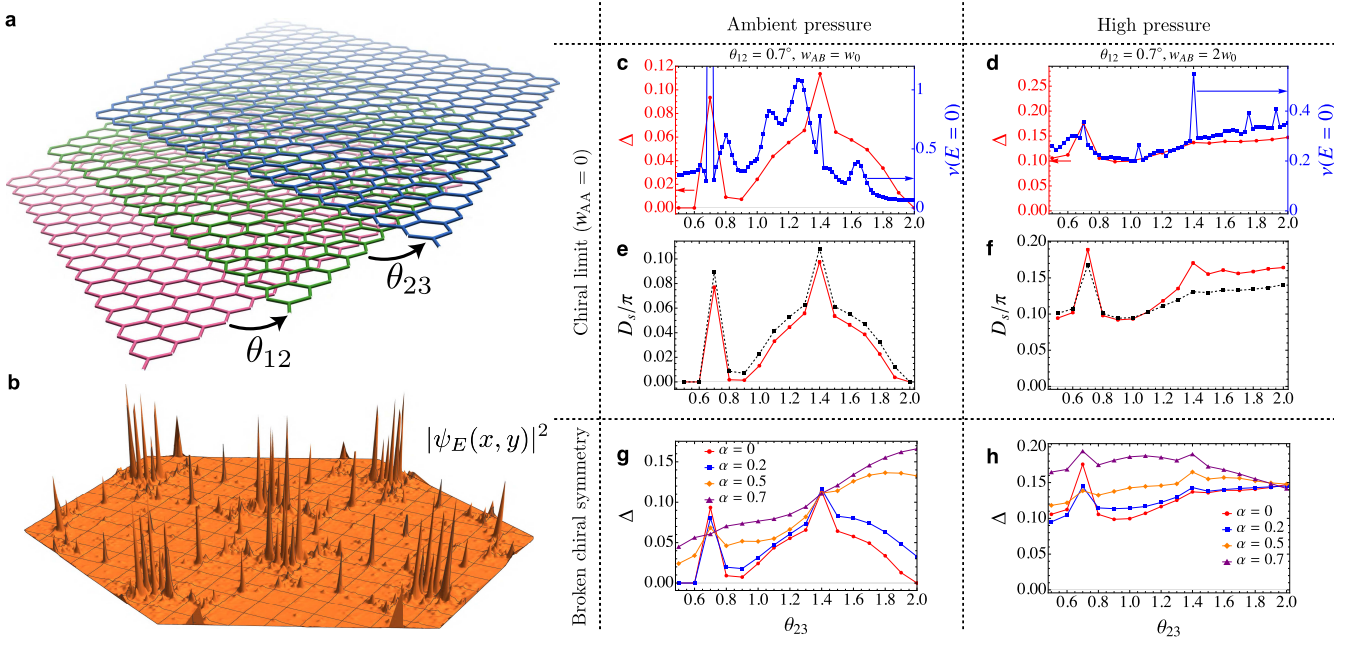


FIG. 1. **Fractal wave functions and robust superconductivity in TTG.** **a**, Illustration of helical twisted trilayer graphene with two independent twist angles θ_{12} and θ_{23} . **b**, A typical quantum-critical, normal-state single-particle wave function in quasiperiodic TTG ($\theta_{12} = 0.5^\circ$ and $\theta_{23} = 0.925^\circ$). The self-similar structure in position space is induced by the quasiperiodicity. **c**, Spatial average of the superconductivity order parameter Δ and density of states near the Fermi energy $\nu(E=0)$ in the chiral limit [28] with $w_{AB} = w_0 = 110$ meV; **d**, Same as **c**, but with doubled interlayer coupling $w_{AB} = 2w_0 = 220$ meV. **e** and **f**, Superfluid stiffness D_s/π (red) in the chiral limit with $w_{AB} = w_0$ and $w_{AB} = 2w_0$, respectively. The black dashed line shows $D_s/\pi = 3\Delta/\pi$, which is the result for an *ideal* Dirac superconductor without moiré potentials [4, 29–31]. **g** and **h**, Superconducting order parameter for the realistic TTG model with broken chiral symmetry ($\alpha \neq 0$, see text) with $w_{AB} = w_0$ and $w_{AB} = 2w_0$, respectively. Δ and D_s/π are given in units of $v_F k_{\theta_{12}} \approx 124$ meV and the attractive interaction is set to be $U = 4v_F k_{\theta_{12}} = 496$ meV. The linear system size is $L = 77$ for **c–h**, while the polynomial order N_C utilized in the kernel polynomial method is 2048 for Δ and 1024 for D_s calculations [32].

SUPERCONDUCTIVITY IN TTG

We focus on helical TTG with independent tunable twist angles θ_{12} and θ_{23} [Fig. 1a]. The quasiperiodicity is governed by the competition of the two moiré scales $L_{12} \sim \sqrt{3}a/\theta_{12}$ and $L_{23} \sim \sqrt{3}a/\theta_{23}$ (small-angle limit; $a \approx 1.42$ Å). In this section we establish the presence and robustness of superconductivity in the resulting inhomogeneous landscape. In the following section, we show that it originates from the quantum-critical normal-state electrons.

The low-energy physics of TTG in valley K is described by the Hamiltonian [10, 36],

$$H_K = \int d^2\mathbf{r} \psi_{K\mathbf{r}}^\dagger h_K(\mathbf{r}) \psi_{K\mathbf{r}}, \quad (1)$$

$$h_K(\mathbf{r}) = [-i\boldsymbol{\sigma} \cdot \nabla + V_{12}(\mathbf{r}) + V_{23}(\mathbf{r})],$$

where $\psi_{K\mathbf{r}}$ is a six-component electronic spinor with sublattice ($\sigma = 1, 2$) and layer indices (1, 2, 3). $V_{12}(\mathbf{r})$ and $V_{23}(\mathbf{r})$ are the interlayer tunneling potentials forming the

top and bottom moiré patterns. $V_{12}(\mathbf{r})$ takes the form

$$V_{12}(\mathbf{r}) = w_{AB} [U_1(\mathbf{r}) t^+ \sigma^+ + U_{-1}(\mathbf{r}) t^+ \sigma^-] + w_{AA} U_0(\mathbf{r}) t^+ + \text{H.c.} \quad (2)$$

Here $U_n(\mathbf{r}) = e^{i\mathbf{q}_1^{(12)} \cdot \mathbf{r}} + e^{-in\phi} e^{i\mathbf{q}_2^{(12)} \cdot \mathbf{r}} + e^{in\phi} e^{i\mathbf{q}_3^{(12)} \cdot \mathbf{r}}$ with $n = 0, \pm 1$, and $t^\pm = \frac{1}{2}(t^1 \pm it^2)$ are 3×3 matrices coupling together layers 1 and 2. In Eq. (2), w_{AA} and w_{AB} are the interlayer tunneling strengths in the AA and AB (Bernal) stacking regions, respectively. The tunneling in the AA region is smaller than that in the AB region due to lattice relaxation effects [37, 38], which can be quantified by the dimensionless parameter $\alpha \equiv w_{AA}/w_{AB} \approx 0.7$. The moiré potential between layers 1 and 2 is characterized by the reciprocal lattice vectors $\mathbf{q}_1^{(12)} = k_{\theta_{12}}(1, 0)$ and $\mathbf{q}_{2,3}^{(12)} = k_{\theta_{12}}(-1/2, \pm\sqrt{3}/2)$, with $k_{\theta_{12}} = 2K \sin(\theta_{12}/2)$. The interlayer coupling V_{23} takes a similar form with $\mathbf{q}_i^{(12)}$ replaced by $\mathbf{q}_i^{(23)}$.

In this paper, we mostly employ a collinear approximation and assume that $\mathbf{q}_i^{(23)} = \mathbf{q}_i^{(12)} \sin \frac{\theta_{23}}{2} / \sin \frac{\theta_{12}}{2}$, in order to access much larger system sizes than the previous work based on a non-collinear model [10]. In other words, we assume that the two adjacent moiré lattices are rota-

tionally aligned (but with quasiperiodic periods). This is justified at small twist angles where the misalignment at the moiré-of-moiré scale [5] is parametrically weak (we check that collinear and non-collinear models agree qualitatively, see below).

The chiral limit with $\alpha = 0$ is believed to capture the key features of the twisted multilayer graphene and is a good starting point for theoretical study [28]. In this limit, $V_{12} + V_{23}$ is exactly a non-Abelian gauge potential and the system mimics the topological *surface states* of a 3D topological superconductor, explained below.

For simplicity, we focus on the simplest conventional scenario for superconductivity: intervalley *s*-wave pairing. (More exotic pairing scenarios are discussed in the conclusion.) We consider a local attractive interaction

$$H_{\text{int}} = -U \int d^2\mathbf{r} \psi_{\mathbf{r}\uparrow}^\dagger \psi_{\mathbf{r}\uparrow} \psi_{\mathbf{r}\downarrow}^\dagger \psi_{\mathbf{r}\downarrow}, \quad (3)$$

and treat it within self-consistent Bogoliubov-de Gennes (BdG) theory to obtain the local superconducting pairing amplitude $\Delta_{\mathbf{r}}$ and density $n_{\mathbf{r}}$. The BdG Hamiltonian is

$$H_{\text{BdG}} = \frac{1}{2} \int d^2\mathbf{r} \chi_{\mathbf{r}}^\dagger h_{\text{BdG}}(\mathbf{r}) \chi_{\mathbf{r}}, \quad (4)$$

where quasiparticles are encoded in the composite spinor $\chi = [\psi_{K\mathbf{r}}, is_2(\psi_{-K\mathbf{r}}^\dagger)^\top]^\top$, the valleys are labeled by $\pm K$, and the BdG Hamiltonian is

$$h_{\text{BdG}}(\mathbf{r}) = \left[h_K(\mathbf{r}) - \frac{U}{2} n_{\mathbf{r}} \right] \mu_3 + \Delta_{\mathbf{r}} \mu_1. \quad (5)$$

In the above, s_i and μ_j respectively denote Pauli matrices acting on spin-1/2 and particle-hole spaces; $-U n_{\mathbf{r}}/2$ is the Hartree shift. The ground-state superconductivity is evaluated self-consistently via the kernel polynomial method (KPM); details of the computational methodology can be found in Refs. [4, 32]. In what follows, we focus on the case of half-filling.

We begin in the chiral limit with standard [36, 37] interlayer couplings $w_{\text{AA}} = 0$ and $w_{\text{AB}} = 110$ meV. The spatially averaged pairing amplitude Δ and zero-energy density of states (DOS) $\nu(E=0)$ are plotted versus twist angle in Fig. 1c. Both the DOS and the pairing amplitude exhibit sharp maxima at commensurate configurations where θ_{23} is an integer multiple of θ_{12} . Away from these special angles, however, the DOS and Δ do not track each other, implying that superconductivity is not simply controlled by flat-band physics. Fig. 1e shows the superfluid stiffness of quasiperiodic TTG. The superfluid stiffness D_s closely follows the analytical prediction expected for an *ideal* Dirac superconductor (without moiré potentials), $D_s/\pi = 3\Delta/\pi$ [4, 29–31]. This behavior shows that the superconductivity in TTG is robust against phase fluctuations and that quasiperiodicity does not degrade phase coherence. The reason for this turns out to be the topology in the TTG Hamiltonian in the chiral limit, which

simulates topological surface states. The normal state is critical, with a conductivity pinned to a universal value $\sigma_n = 3e^2/\pi h$ reflected in the superfluid stiffness [4]. This finite and angle-insensitive conductivity prevents the suppression of D_s that would normally arise from strong spatial inhomogeneity [21], allowing superconductivity to remain robust across a broad range of twist angles.

All of this physics is enhanced and changes qualitatively when we simulate applied pressure by doubling the interlayer coupling to $w_{\text{AA}} = 0$, $w_{\text{AB}} = 220$ meV, as shown in Fig. 1d. Such enhanced couplings are experimentally accessible using realistic hydrostatic pressures [33–35]. Commensurate configurations still produce noticeable peaks in the average Δ , but the pairing amplitude becomes far more uniform across twist-angle space. This robustness implies that increasing w_{AB} removes the angle sensitivity and thus stabilizes superconductivity across twist angles. Similar behavior is seen with the superfluid stiffness in Fig. 1f, which still roughly follows $D_s/\pi = 3\Delta/\pi$ implying it too is angle-robust.

In realistic samples, although Bernal (AB) stackings have a smaller interlayer spacing due to lattice relaxation and $w_{\text{AB}} > w_{\text{AA}}$ [37, 38], w_{AA} never vanishes. The w_{AA} term breaks both the approximate chiral symmetry [28] of the continuum model and the link to topological surfaces, but it does not gap the Dirac points or generate a *Chern mass*. As we explain below, the finite-energy wave functions of the chiral model in the normal state show critical fluctuations consistent with the integer quantum Hall plateau transition. In the absence of nonzero average Berry curvature, this criticality is robust [39]. Fig. 1g,h show the pairing amplitude of TTG with broken chiral symmetry ($\alpha \neq 0$) for $w_{\text{AB}} = w_0$ and $w_{\text{AB}} = 2w_0$. At commensurate angles, superconductivity is suppressed or unchanged by the chiral symmetry-breaking term (except for $\alpha = 0.7$ and $w_{\text{AB}} = 2w_0$) compared to the chiral limit. By contrast, for incommensurate angles, where quasiperiodicity is strongest, the symmetry-breaking term *further enhances* the pairing amplitude. This behavior demonstrates that the superconductivity supported by the quasiperiodic normal state is not tied to fine-tuned chiral symmetry. Rather, the mechanism that stabilizes pairing in TTG remains effective even when AA tunneling is included at realistic strengths.

The robust superfluid stiffness in the presence of quasiperiodicity indicates that the normal state does not Anderson-localize but remains in a critical conducting regime. We now show TTG effectively simulates a class-AIII topological surface that exhibits spectrum-wide quantum criticality, yielding multifractal wave functions and near-universal longitudinal conductivity.

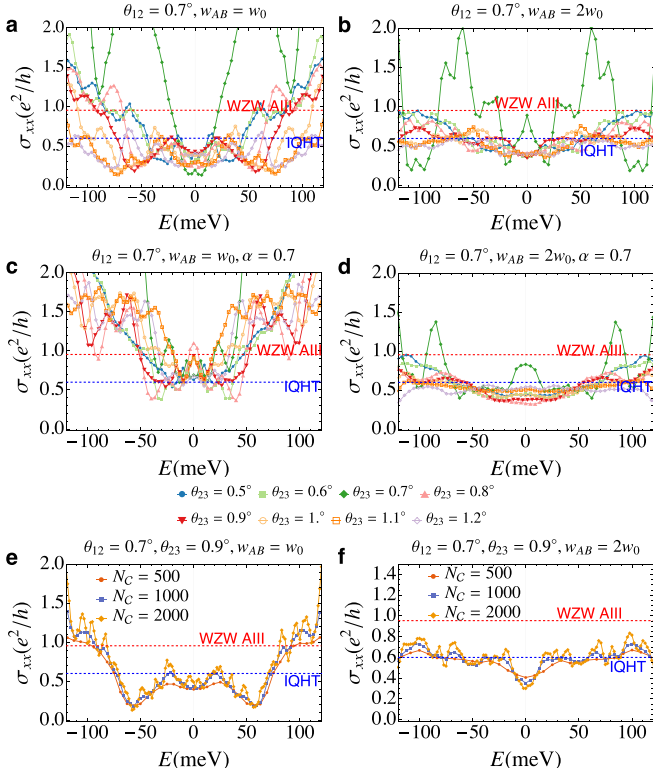


FIG. 2. **Normal-state conductivity in TTBG.** **a–b**, Conductivity σ_{xx} of TTBG in the chiral limit versus eigenstate energy E with $w_{AB} = w_0$ and $w_{AB} = 2w_0$, respectively. **c–d**, Including realistic chiral symmetry breaking $\alpha = 0.7$. **e–f**, Conductivity evaluated with different KPM polynomial orders N_C . The red and blue dashed lines show reference values for critical states predicted to occur in class AIII [23, 40]: WZW [zero energy, $3e^2/(\pi h)$] and IQHT [finite energy, $\approx 0.6e^2/h$]. The linear system size $L = 308$.

QUASIPERIODIC CRITICALITY

Surfaces of 3D bulk topological phases [41, 42] exhibit massless two-dimensional (2D) Dirac electrons with *unique* properties not usually realizable in any crystalline or quasiperiodic 2D system with local hopping [43, 44]. However, they can be *effectively simulated* by such a system if intervalley scattering can be neglected. This is the case with small twist-angle multilayer graphene [4].

In the chiral limit and neglecting intervalley coupling, the Dirac electrons in the normal state of TTBG simulate the surface of a class-AIII topological phase [23, 24, 41]. This surface is predicted to exhibit zero-energy states that are topologically protected from Anderson localization and that possess a universal longitudinal conductivity [40]. Recently it was hypothesized and numerically demonstrated that the finite-energy states of a class-AIII surface with symmetry-preserving disorder exhibit a remarkable “spectrum-wide quantum criticality” (SWQC) [24]. Disorder and topology induce a “multifractal metal”—a whole tower of robust finite-energy states [23, 39] with univer-

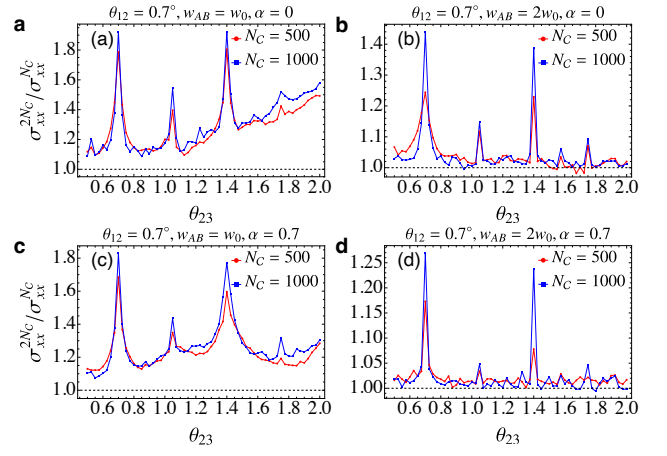


FIG. 3. **The ratio of normal-state conductivity evaluated with $2N_C$ and N_C .** **a–b**, The ratio $\sigma_{xx}^{2N_C}/\sigma_{xx}^{N_C}$ of TTBG in the chiral limit with $w_{AB} = w_0$ and $w_{AB} = 2w_0$, respectively. **c–d**, The ratio for TTBG with chiral symmetry breaking. The ratio is expected to be ≈ 1 (dashed line) for critical states, and deviates from 1 for ballistic transport. The peaks in the ratio correspond to commensurate twist angles. Results are averaged over the energy window $v_F k_{\theta_{12}}(-1, 1)$ and $L = 308$.

sal statistics consistent with the integer quantum Hall plateau transition (IQHT), itself a 2D topological quantum phase transition. By contrast, in the quantum Hall effect critical IQHT states occur only at isolated energies.

Quasiperiodicity can play the same role as symmetry-preserving disorder. In TTBG, the AIII-like symmetry is approximately preserved by the suppression of intervalley scattering and the nature of tunneling between layers, allowing it to realize the SWQC scenario involving IQHT states across the energy spectrum. A key attribute of this phenomenology is that the normal-state conductivity should be of order e^2/h for a wide swath of eigenstate energies E . The normal-state conductivity (in units of e^2/h) is given by the Kubo formula,

$$\sigma_{xx}(E) = \frac{2\pi^2}{L^2} \text{Tr} [j_x \delta(E - h_K) j_x \delta(E - h_K)]. \quad (6)$$

Here j_x is the current operator in x -direction and L is the linear system size. We calculate the Kubo conductivity using KPM [32, 45], and access system sizes comparable to experimental samples. The normal-state conductivity $\sigma_{xx}(E)$ of TTBG is shown in Fig. 2. In the chiral limit, the calculated TTBG conductivity fluctuates around the average IQHT critical conductivity $\approx 0.6e^2/h$ [46, 47] for incommensurate twist angles [Fig. 2a], consistent with the topological SWQC scenario. At $\theta_{12} = \theta_{23} = 0.7^\circ$, the collinear model is commensurate with a finite moiré period, and the conductivity well exceeds this critical value. This is consistent with ballistic transport broadened by the KPM method (see below). Increasing the interlayer tunneling strength to $w_{AB} = 2w_0$ [Fig. 2b], the chiral TTBG model conductivity locks closely to the

IQHT value with weaker fluctuations over a wider range of energy, consistent with the superconducting behavior seen in Fig. 1d,f.

Incorporating realistic chiral symmetry breaking ($\alpha \approx 0.7$) increases the conductivity in quasiperiodic TTG with $w_{AB} = w_0$ [Fig. 2c], and weakens the criticality. By contrast, conductivity is stabilized near the IQHT value when the interlayer tunneling is doubled, even with broken chiral symmetry [Fig. 2d]. These results show that TTG at normal pressure ($w_{AB} = w_0$) resides in a crossover regime featuring both ballistic and critical states, where wave functions are sensitive to microscopic details, especially chiral symmetry breaking. The possibility of ballistic states despite broken translational symmetry is a well-known feature of quasiperiodic systems [20]. Fig. 2d shows that the topological criticality is uniformly stabilized with increasing interlayer tunneling, as achievable via applied pressure, even without chiral symmetry—again complementary to the enhanced superconducting behavior seen in Fig. 1h.

To distinguish between ballistic and critical or diffusive regimes in quasiperiodic systems, KPM conductivity calculations provide a natural diagnostic. When using KPM on Eq. (6), the conductivity is naturally regulated by a lifetime $\tau_{\text{KPM}} \sim N_C$, where N_C is the order of the polynomials employed. In critical or diffusive regimes, the system develops a physical lifetime τ_{phys} due to elastic impurity scattering, which is independent of N_C . When $\tau_{\text{KPM}} \gtrsim \tau_{\text{phys}}$ the conductivity will plateau with increasing N_C while developing noisy state-to-state fluctuations for very large N_C , see Fig. 2e and f. For ballistic states, however, the conductivity is (artificially) determined by τ_{KPM} and increases with N_C without saturating.

Fig. 3 shows the ratio of σ_{xx} evaluated with different N_C plotted versus twist angle. The ratio is close to unity at incommensurate angles and peaks around the commensurate ones. This shows that quasiperiodic TTG is critical, while the commensurate angles are ballistic. At large θ_{23} , quasiperiodic TTG also becomes ballistic as the third graphene layer effectively decouples from the other two. With chiral symmetry breaking [Fig. 3c], the peaks are broadened, indicating weakened criticality. Instead, the ratio collapses to 1 for incommensurate twist angles and shows narrow peaks at commensurate angles [Fig. 3b and d] when interlayer coupling is doubled, consistent with enhanced criticality in the conductivity, Fig. 2d.

MODEL COMPARISON

In TTG, each layer’s momentum-space Dirac lattice is rotated by a different twist angle. As two layers are twisted relative to each other, both the magnitude and direction of the moiré reciprocal vectors change; the collinear model neglects the directional mismatch. Keeping both magnitude and direction mismatch leads to a

“non-collinear” model [10] which is more computationally intensive than the collinear model employed above. However, for small twist angles the directional mismatch between layers is small relative to the magnitude mismatch, justifying the collinear approximation. Here, we show both the collinear model and the non-collinear model capture the same underlying physics.

We first show that both models predict qualitatively the same multifractal behaviors for critical wave functions at zero energy $E = 0$. Wave function criticality is characterized by the scaling of the inverse participation ratio (IPR) $P_2 \equiv \sum_{\mathbf{r}} |\psi_{\mathbf{r}}|^4 \sim L^{-\tau_2}$, where L is the linear system size and τ_2 is the multifractal dimension in real space, defined by \mathbf{r} . We can also define a momentum-space IPR by replacing \mathbf{r} with \mathbf{k} . In the collinear model, we directly access real-space wave functions and extract the real-space exponent τ_2 , see Fig. 4a. For $\theta_{12} + \theta_{23} \lesssim 1.6^\circ$ and away from commensurate angles we find $\tau_2 \lesssim 1.8$, indicating multifractal, critical states. Along the commensurate lines (white dashed lines), the system becomes periodic in the continuum limit, and $\tau_2 \approx 2$, consistent with plane-wave-like states. Similarly, in the strongly asymmetric limit $\theta_{12} \gg \theta_{23}$, the system effectively reduces to a weakly coupled twisted bilayer and a monolayer. Approximate moiré periodicity is restored, and wave functions again become extended, consistent with ballistic transport.

In the non-collinear model [32], we have direct access to the momentum-space IPR, which defines the momentum-space multifractal exponent τ_2^k . With the momentum-space IPR, the trends are inverted: plane-wave-like states correspond to small τ_2^k , while strongly localized states yield $\tau_2^k \approx 2$. As shown in Fig. 4b, the non-collinear model exhibits a broad critical region with $\tau_2^k \sim 1$ in the same triangular domain of twist angles where the collinear model has real-space multifractality. In the large-angle, weakly coupled regimes, τ_2^k is strongly suppressed, indicating extended (ballistic) states in agreement with the collinear model. The two descriptions therefore identify the same critical and ballistic regions in twist-angle space, despite their different microscopic implementations.

To further confirm the agreement between the two models, we compare their transport properties. Fig. 5 shows the longitudinal conductivity $\sigma_{xx}(E)$, obtained from the non-collinear model in the chiral limit for $w_{AB} = 220$ meV at fixed $\theta_{12} = 0.7^\circ$ as a function of θ_{23} . The conductivity is evaluated using the Kubo formula with an energy smearing of 5 meV, analogous to the KPM calculations in the collinear model. Away from commensurate angles, σ_{xx} is nearly energy independent and fluctuates around the integer quantum Hall transition value $\sigma_{xx} \approx 0.6 e^2/h$ (black dashed line), signaling a scale-invariant critical metal. In contrast, near commensurate twist-angle combinations, σ_{xx} exhibits pronounced peaks and dips, reflecting the crossover to ballistic behavior in periodic or nearly periodic configurations. This pattern closely mirrors the conductivity maps and the N_C -scaling diagnostics ob-

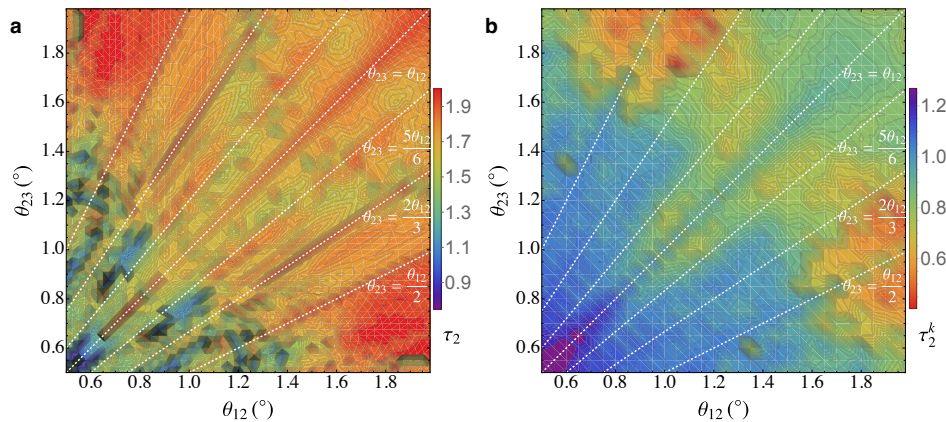


FIG. 4. **Multifractal dimension in collinear and non-collinear model for TTG.** Here we show results in the chiral limit with $w_{AB} = w_0$. **a**, Real-space multifractal dimension τ_2 for the $E = 0$ wave function in TTG evaluated with the collinear model. **b**, Momentum-space multifractal dimension τ_2^k in TTG evaluated with the non-collinear model. Small τ_2 and large τ_2^k indicate a quantum-critical state. The multifractal dimensions in both models reflect the same criticality behavior in the normal state of TTG.

tained from the collinear model [Figs. 2 and 3].

These comparisons validate the collinear model for the long-wavelength physics relevant here. Both models identify the same incommensurate twist angle configurations which realize a critical metal with $\sigma_{xx} \sim e^2/h$, multifractal wave functions, and robust resistance to localization. Both also recover ballistic behavior along commensurate lines and in the weakly coupled limits.

CONCLUSION

We have shown that TTG with two generic independent twist angles can realize a quantum-critical metallic phase in its normal state. As a consequence, it also hosts robust superconductivity over a broad range of twist-angle combinations and interlayer couplings. In the normal-state critical metal, single-particle wave functions are multifrac-

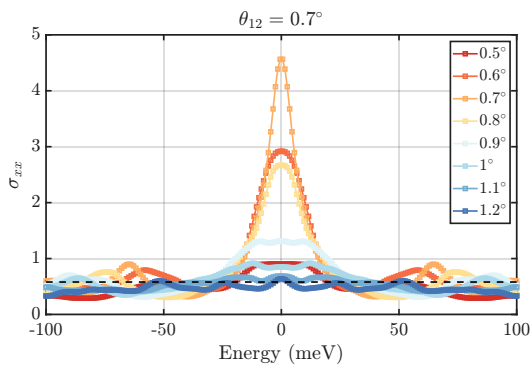


FIG. 5. Conductivity in units of e^2/h obtained from the non-collinear model in the chiral limit for $w_{AB} = 220$ meV with $\theta_{12} = 0.7^\circ$ and varying θ_{23} . The smearing width is 5 meV. The black dashed line is 0.6, which is the IQHT value.

tal and the longitudinal conductivity remains of the order of the universal average IQHT value $\sim 0.6e^2/h$ across a wide energy window.

The key insight is the identification of the effective TTG model with that of exotic topological surface states, predicted to demonstrate robust quantum criticality in the *spatially aperiodic structure* of wave functions. Our results show that quasiperiodicity, a feature generic in multilayer moiré materials, can serve as a source of momentum mixing that reveals the effective topology and enables superconductivity without fine-tuning or degradation of the superfluid stiffness. Moreover, we show that increasing the interlayer coupling strength stabilizes quantum criticality in the normal state and further enhances superconductivity. Therefore, we predict that stronger superconductivity occurs in quasiperiodic TTG if high pressure is applied.

The low energy physics of other moiré materials, such as transition-metal dichalcogenide (TMD) multilayers, is not described by Dirac fermions as in multilayer graphene. Therefore, the specific class-AIII/IQHT-like route to quantum criticality is not expected to apply to these moiré materials. Nonetheless, new kinds of quantum criticality could arise in quasiperiodic TMD multilayers and it is interesting to clarify whether it favors robust superconductivity.

We have limited ourselves to conventional s -wave intervalley pairing in order to focus on the role of the normal state. Strong correlations could produce exotic nodal pairing, as occurs in the d -wave cuprates and as suggested by recent experiments in moiré graphene [9, 48]. On one hand, the absence of Anderson's theorem for non- s -wave superconductivity seems to imply strong vulnerability to translational symmetry breaking [2]. At the same time, the strong electronic inhomogeneity observed in the

cuprates [49] suggests that the interplay between nodal pairing, translational symmetry breaking, and strong correlations involves as-yet undiscovered physics. Wedding these elements to the topological mechanisms discussed here is an important direction for future work.

This work was supported by the Welch Foundation Grant No. C-1809 (X.Z. and M.S.F.). X.Z. also acknowledges support from Paul Scherrer Institute, and from the ERC under the EU's Horizon 2020 research and innovation program, Grant Agreement 810451. J.H.W. acknowledges support from the National Science Foundation under Grant Number DMR-2238895. Z.Z. acknowledges support from a Stanford Science fellowship and a startup fund at Boston College. Z.Z. and J.H.W. acknowledge Aspen Center for Physics where part of this work was performed, which is supported by a National Science Foundation grant PHY-2210452.

-
- [1] Zhang, X. & Foster, M. S. Enhanced amplitude for superconductivity due to spectrum-wide wave function criticality in quasiperiodic and power-law random hopping models. *Phys. Rev. B* **106**, L180503 (2022). URL <https://link.aps.org/doi/10.1103/PhysRevB.106.L180503>.
- [2] Ticea, N. S., May-Mann, J., Xiao, J., Berg, E. & Devakul, T. Stability of quasiperiodic superconductors. *Phys. Rev. B* **110**, L060501 (2024). URL <https://link.aps.org/doi/10.1103/PhysRevB.110.L060501>.
- [3] Uri, A. *et al.* Superconductivity and strong interactions in a tunable moiréquasicrystal. *Nature* **620**, 762–767 (2023). URL <https://doi.org/10.1038/s41586-023-06294-z>.
- [4] Zhang, X., Wilson, J. H. & Foster, M. S. Critical filaments and superconductivity in quasiperiodic twisted bilayer graphene. *Phys. Rev. B* **111**, 024207 (2025). URL <https://link.aps.org/doi/10.1103/PhysRevB.111.024207>.
- [5] Zhu, Z., Cazeaux, P., Luskun, M. & Kaxiras, E. Modeling mechanical relaxation in incommensurate trilayer van der waals heterostructures. *Phys. Rev. B* **101**, 224107 (2020). URL <https://link.aps.org/doi/10.1103/PhysRevB.101.224107>.
- [6] Turkel, S. *et al.* Orderly disorder in magic-angle twisted trilayer graphene. *Science* **376**, 193–199 (2022). URL <https://www.science.org/doi/abs/10.1126/science.abk1895>. <https://www.science.org/doi/pdf/10.1126/science.abk1895>.
- [7] Craig, I. M. *et al.* Local atomic stacking and symmetry in twisted graphene trilayers. *Nature Materials* **23**, 323–330 (2024). URL <https://doi.org/10.1038/s41563-023-01783-y>.
- [8] Hoke, J. C. *et al.* Imaging supermoire relaxation and conductive domain walls in helical trilayer graphene. *arXiv preprint arXiv:2410.16269* (2024).
- [9] Park, J. M., Sun, S., Watanabe, K., Taniguchi, T. & Jarillo-Herrero, P. Experimental evidence for nodal superconducting gap in moiré graphene. *Science* **0**, eadv8376. URL <https://www.science.org/doi/abs/10.1126/science.adv8376>. <https://www.science.org/doi/pdf/10.1126/science.adv8376>.
- [10] Zhu, Z., Carr, S., Massatt, D., Luskun, M. & Kaxiras, E. Twisted Trilayer Graphene: A Precisely Tunable Platform for Correlated Electrons. *Phys. Rev. Lett.* **125**, 116404 (2020). URL <https://link.aps.org/doi/10.1103/PhysRevLett.125.116404>.
- [11] Devakul, T. *et al.* Magic-angle helical trilayer graphene. *Science Advances* **9**, eadi6063 (2023). URL <https://www.science.org/doi/abs/10.1126/sciadv.adi6063>. <https://www.science.org/doi/pdf/10.1126/sciadv.adi6063>.
- [12] Mao, Y., Guerci, D. & Mora, C. Supermoiré low-energy effective theory of twisted trilayer graphene. *Phys. Rev. B* **107**, 125423 (2023). URL <https://link.aps.org/doi/10.1103/PhysRevB.107.125423>.
- [13] Guerci, D., Mao, Y. & Mora, C. Chern mosaic and ideal flat bands in equal-twist trilayer graphene. *Phys. Rev. Res.* **6**, L022025 (2024). URL <https://link.aps.org/doi/10.1103/PhysRevResearch.6.L022025>.
- [14] Yang, C., May-Mann, J., Zhu, Z. & Devakul, T. Multi-moiré trilayer graphene: Lattice relaxation, electronic structure, and magic angles. *Phys. Rev. B* **110**, 115434 (2024). URL <https://link.aps.org/doi/10.1103/PhysRevB.110.115434>.
- [15] Zhang, X. *et al.* Correlated Insulating States and Transport Signature of Superconductivity in Twisted Trilayer Graphene Superlattices. *Phys. Rev. Lett.* **127**, 166802 (2021). URL <https://link.aps.org/doi/10.1103/PhysRevLett.127.166802>.
- [16] Xia, L.-Q. *et al.* Magic continuum in multi-moiré twisted trilayer graphene (2025). URL <https://arxiv.org/abs/2509.03583>. 2509.03583.
- [17] Hoke, J. C. *et al.* Linking thermodynamic correlation signatures and superconductivity in twisted trilayer graphene. *arXiv preprint arXiv:2509.07977* (2025).
- [18] Xia, L.-Q. *et al.* Topological bands and correlated states in helical trilayer graphene. *Nature Physics* **21**, 239–244 (2025). URL <https://doi.org/10.1038/s41567-024-02731-6>.
- [19] Xie, Y. *et al.* Strong interactions and isospin symmetry breaking in a supermoiré lattice. *Science* **389**, 736–740 (2025). URL <https://www.science.org/doi/abs/10.1126/science.adl2544>. <https://www.science.org/doi/pdf/10.1126/science.adl2544>.
- [20] Sokoloff, J. B. Unusual band structure, wave functions and electrical conductance in crystals with incommensurate periodic potentials. *Phys. Rep.* **126**, 189 (1985). URL [https://doi.org/10.1016/0370-1573\(85\)90088-2](https://doi.org/10.1016/0370-1573(85)90088-2).
- [21] Trivedi, N., Scalettar, R. T. & Randeria, M. Superconductor-insulator transition in a disordered electronic system. *Phys. Rev. B* **54**, R3756 (1996). URL <https://link.aps.org/doi/10.1103/PhysRevB.54.R3756>.
- [22] Fan, Z., Chern, G.-W. & Lin, S.-Z. Enhanced superconductivity in quasiperiodic crystals. *Phys. Rev. Res.* **3**, 023195 (2021). URL <https://link.aps.org/doi/10.1103/PhysRevResearch.3.023195>.
- [23] Sbierski, B., Karcher, J. F. & Foster, M. S. Spectrum-Wide Quantum Criticality at the Surface of Class AIII Topological Phases: An “Energy Stack” of Integer Quantum Hall Plateau Transitions. *Phys. Rev. X* **10**, 021025 (2020). URL <https://link.aps.org/doi/10.1103/PhysRevX.10.021025>.
- [24] Karcher, J. F. & Foster, M. S. How spectrum-wide quantum criticality protects surface states of topological superconductors from Anderson localization: Quantum Hall plateau transitions (almost)

- all the way down. *Annals of Physics* **435**, 168439 (2021). URL <https://www.sciencedirect.com/science/article/pii/S0003491621000452>. Special Issue on Localisation 2020.
- [25] Evers, F. & Mirlin, A. D. Anderson transitions. *Rev. Mod. Phys.* **80**, 1355 (2008). URL <https://link.aps.org/doi/10.1103/RevModPhys.80.1355>.
- [26] Feigel'man, M. V., Ioffe, L. B., Kravtsov, V. E. & Yuzbashyan, E. A. Eigenfunction Fractality and Pseudogap State near the Superconductor-Insulator Transition. *Phys. Rev. Lett.* **98**, 027001 (2007). URL <https://link.aps.org/doi/10.1103/PhysRevLett.98.027001>.
- [27] Tezuka, M. & García-García, A. M. Stability of the superfluid state in a disordered one-dimensional ultracold fermionic gas. *Phys. Rev. A* **82**, 043613 (2010). URL <https://link.aps.org/doi/10.1103/PhysRevA.82.043613>.
- [28] Tarnopolsky, G., Kruchkov, A. J. & Vishwanath, A. Origin of Magic Angles in Twisted Bilayer Graphene. *Phys. Rev. Lett.* **122**, 106405 (2019). URL <https://link.aps.org/doi/10.1103/PhysRevLett.122.106405>.
- [29] Kopnin, N. B. & Sonin, E. B. BCS Superconductivity of Dirac Electrons in Graphene Layers. *Phys. Rev. Lett.* **100**, 246808 (2008). URL <https://link.aps.org/doi/10.1103/PhysRevLett.100.246808>.
- [30] Uchoa, B. & Castro Neto, A. H. Comment on “BCS Superconductivity of Dirac Electrons in Graphene Layers”. *Phys. Rev. Lett.* **102**, 109701 (2009). URL <https://link.aps.org/doi/10.1103/PhysRevLett.102.109701>.
- [31] Kopnin, N. B. & Sonin, E. B. Kopnin and Sonin Reply. *Phys. Rev. Lett.* **102**, 109702 (2009). URL <https://link.aps.org/doi/10.1103/PhysRevLett.102.109702>.
- [32] See Supplemental Material at [URL] for a details of the KPM implementation, non-collinear model, and additional conductivity and density of states data.
- [33] Carr, S., Fang, S., Jarillo-Herrero, P. & Kaxiras, E. Pressure dependence of the magic twist angle in graphene superlattices. *Phys. Rev. B* **98**, 085144 (2018). URL <https://link.aps.org/doi/10.1103/PhysRevB.98.085144>.
- [34] Yankowitz, M. *et al.* Tuning superconductivity in twisted bilayer graphene. *Science* **363**, 1059–1064 (2019). URL <https://www.science.org/doi/abs/10.1126/science.aav1910>. <https://www.science.org/doi/pdf/10.1126/science.aav1910>.
- [35] Wang, Y. *et al.* Pressure-Driven Moiré Potential Enhancement and Tertiary Gap Opening in Graphene/h-BN Heterostructure. *Phys. Rev. Lett.* **135**, 046303 (2025). URL <https://link.aps.org/doi/10.1103/xs5j-hp3p>.
- [36] Bistrizter, R. & MacDonald, A. H. Moiré bands in twisted double-layer graphene. *Proceedings of the National Academy of Sciences* **108**, 12233–12237 (2011). URL <https://www.pnas.org/doi/abs/10.1073/pnas.1108174108>. <https://www.pnas.org/doi/pdf/10.1073/pnas.1108174108>.
- [37] Nam, N. N. T. & Koshino, M. Lattice relaxation and energy band modulation in twisted bilayer graphene. *Phys. Rev. B* **96**, 075311 (2017). URL <https://link.aps.org/doi/10.1103/PhysRevB.96.075311>.
- [38] Carr, S. *et al.* Relaxation and domain formation in incommensurate two-dimensional heterostructures. *Phys. Rev. B* **98**, 224102 (2018). URL <https://link.aps.org/doi/10.1103/PhysRevB.98.224102>.
- [39] Altland, A. *et al.* Fragility of Surface States in Non-Wigner-Dyson Topological Insulators. *Phys. Rev. X* **14**, 011057 (2024). URL <https://link.aps.org/doi/10.1103/PhysRevX.14.011057>.
- [40] Ludwig, A. W. W., Fisher, M. P. A., Shankar, R. & Grinstein, G. Integer quantum Hall transition: An alternative approach and exact results. *Phys. Rev. B* **50**, 7526 (1994). URL <https://link.aps.org/doi/10.1103/PhysRevB.50.7526>.
- [41] Schnyder, A. P., Ryu, S., Furusaki, A. & Ludwig, A. W. W. Classification of topological insulators and superconductors in three spatial dimensions. *Phys. Rev. B* **78**, 195125 (2008). URL <https://link.aps.org/doi/10.1103/PhysRevB.78.195125>.
- [42] Kitaev, A. Periodic table for topological insulators and superconductors. *AIP Conf. Proc.* **1134** (2009). URL <https://doi.org/10.1063/1.3149495>.
- [43] Redlich, A. N. Gauge Noninvariance and Parity Nonconservation of Three-Dimensional Fermions. *Phys. Rev. Lett.* **52**, 18 (1984). URL <https://link.aps.org/doi/10.1103/PhysRevLett.52.18>.
- [44] Semenoff, G. W. Condensed-Matter Simulation of a Three-Dimensional Anomaly. *Phys. Rev. Lett.* **53**, 2449 (1984). URL <https://link.aps.org/doi/10.1103/PhysRevLett.53.2449>.
- [45] Weiße, A., Wellein, G., Alvermann, A. & Fehske, H. The kernel polynomial method. *Rev. Mod. Phys.* **78**, 275–306 (2006). URL <https://link.aps.org/doi/10.1103/RevModPhys.78.275>.
- [46] Jovanović, B. & Wang, Z. Conductance Correlations near Integer Quantum Hall Transitions. *Phys. Rev. Lett.* **81**, 2767–2770 (1998). URL <https://link.aps.org/doi/10.1103/PhysRevLett.81.2767>.
- [47] Schweitzer, L. & Markoš, P. Universal Conductance and Conductivity at Critical Points in Integer Quantum Hall Systems. *Phys. Rev. Lett.* **95**, 256805 (2005). URL <https://link.aps.org/doi/10.1103/PhysRevLett.95.256805>.
- [48] Oh, M. *et al.* Evidence for unconventional superconductivity in twisted bilayer graphene. *Nature* **600**, 240–245 (2021). URL <https://doi.org/10.1038/s41586-021-04121-x>.
- [49] Fujita, K. *et al.* Spectroscopic imaging stm studies of electronic structure in both the superconducting and pseudogap phases of underdoped cuprates. In Dobrosavljević, v., Trivedi, N. & Valles Jr., J. M. (eds.) *Conductor-Insulator Quantum Phase Transitions*, 459–491 (Oxford University Press, Oxford, England, 2012).

Supplemental Material: Twisted Trilayer Graphene, Quasiperiodic Superconductor

Xinghai Zhang,¹ Ziyang Zhu,² Justin H. Wilson,^{3,4} and Matthew S. Foster^{1,5}

¹*Department of Physics and Astronomy, Rice University, Houston, Texas 77005, USA*

²*Department of Physics, Boston College, 140 Commonwealth Avenue Chestnut Hill, MA 02467, USA*

³*Department of Physics and Astronomy, Louisiana State University, Baton Rouge, LA 70803, USA*

⁴*Center for Computation and Technology, Louisiana State University, Baton Rouge, LA 70803, USA*

⁵*Rice Center for Quantum Materials, Rice University, Houston, Texas 77005, USA*

(Dated: December 30, 2025)

CONTENTS

I. Kernel Polynomial Method	1
II. Conductivity of Helical Twisted Trilayer Graphene	2
A. Conductivity in Collinear Model	2
B. Conductivity in Non-Collinear Model	7
III. Density of States in Helical Twisted Trilayer Graphene	8
References	13

The supplemental material is organized as follows: In Sec. I, we provide the computational details of the kernel polynomial method in the collinear model. In Sec. II, we show detailed information on the normal conductivity of helical TTG with varying twist angles, pressure and chiral symmetry breaking term. We also compare the conductivity obtained with the collinear model and non-collinear model. In Sec. III, we show the density of states (DOS) in helical TTG obtained with the collinear model.

I. KERNEL POLYNOMIAL METHOD

In this work, we use the numerically exact kernel polynomial method (KPM) [S1] to evaluate the superconductivity, superfluid stiffness, density of states, normal state wave functions, and conductivity in the collinear model. In KPM, the physical quantities are expanded in the Chebyshev polynomial basis, and kernels are introduced to suppress the Gibbs oscillation near singularities. The key insight is that one can write

$$\delta(E - E') = \frac{1}{\pi\sqrt{1 - E^2}} \left[T_0(E)T_0(E') + 2 \sum_{n=1}^{\infty} T_n(E)T_n(E') \right],$$

and using this as a base, one can create a whole class of Kernels where the sum is cutoff

$$K_{N_c}(E, E') = \frac{1}{\pi\sqrt{1 - E^2}} \left[g_{0,N_c} T_0(E)T_0(E') + 2 \sum_{n=1}^{N_c} g_{n,N_c} T_n(E)T_n(E') \right].$$

Here $T_n(E) = \cos(n \arccos(E))$ is the Chebyshev polynomial, and the K_{N_c} gives a smooth broadening of the δ -function. In the limit as $N_c \rightarrow \infty$ it should converge to $\delta(E - E')$ and one has freedom to choose the g_{n,N_c} for various properties (like positive definite or to minimize the width); for most purposes the Jackson kernel [S1] is appropriate and has these properties. Any function $f(E') = \frac{1}{\pi\sqrt{1 - (E')^2}} [\mu_0 T_0(E') + 2 \sum_{n=1}^{\infty} \mu_n T_n(E')]$ can be approximated by a convolution

$$f_{N_c}(E) = \int_{-1}^1 dE' K_{N_c}(E, E') f(E') = \frac{1}{\pi\sqrt{1 - E^2}} \left[g_{0,N_c} \mu_0 T_0(E) + \sum_{n=1}^{N_c} g_{n,N_c} \mu_n T_n(E) \right]$$

(Note that energies are normalized to be $E \in (-1, 1)$ to satisfy the Chebyshev polynomials.) Since K_{N_C} represents a broadened δ -function, we can use it elsewhere, for example in the expression for the conductivity

$$\sigma_{xx}(E) = \frac{2\pi^2}{L^2} \text{Tr} [j_x \delta(E - H) j_x \delta(E - H)] . \quad (\text{S1})$$

$$\approx \frac{2\pi^2}{L^2} \text{Tr} [j_x K_{N_C}(E, H) j_x K_{N_C}(E, H)] . \quad (\text{S2})$$

The power of this method is that it only involves polynomials of h_K and those polynomials are related to each other by a recurrence relation; thus, the method only involves the action of $H|\psi\rangle$ and is highly efficient when the Hamiltonian H is sparse, which enables large-scale calculation compared to diagonalizing the Hamiltonian. In the self-consistent BdG calculation for superconductivity, while the Hamiltonian is no longer sparse, we can still perform the action of the kinetic term and interaction term on the momentum-space and real-space wave functions separately. The real-space wave function can then be obtained from the momentum space one via fast Fourier transform or vice versa [S2]. The superconductivity data in Fig. 1 is calculated with KPM on a 77×77 lattice.

The normal-state conductivity in Figs. 2 and 3 of the main text are evaluated with KPM implementation of the Kubo formula in Eq. (6) of the main text. We use the standard stochastic evaluation of the trace and perform the calculation on a 308×308 lattice. We use the filter and shake method [S2] to calculate the wave function in Fig. 4a, which is performed on a 220×220 lattice.

II. CONDUCTIVITY OF HELICAL TWISTED TRILAYER GRAPHENE

A. Conductivity in Collinear Model

Figs. S1 and S2 show the normal state conductivity in chiral-limit TTG at ambient and high pressure, respectively. The conductivity is calculated with the collinear model of TTG using the KPM implementation of the Kubo formula [Eq. (6) in main text]. At ambient pressure ($w = w_0$), the conductivity shows quantum criticality at incommensurate angles with $\theta' \lesssim 1.2^\circ$, which is reflected by the order of e^2/h value and conductivity convergence with varying order of polynomials N_C . The non-convergence of σ_{xx} at commensurate angles and large θ' reflects the ballistic transport in the periodic limit. By increasing the pressure ($w = 2w_0$), the quantum criticality is enhanced and σ_{xx} shows a constant value in a wide energy window (spectrum-wide quantum criticality, SWQC). The value σ_{xx} closely follows that of IQHT state ($\sigma_{\text{IQHT}} \approx 0.6e^2/h$), which is consistent with the class AIII symmetry of the normal state.

Figs. S3 and S4 shows the ambient and high-pressure conductivity with chiral symmetry breaking ($\alpha \neq 0$). At ambient pressure ($w = w_0$), the chiral symmetry breaking term weakens the quantum criticality and the conductivity σ_{xx} deviates from that of IQHT state. However, the quantum criticality is robust against chiral symmetry breaking at high pressure ($w = 2w_0$), and the conductivity still follows that of IQHT value in quasiperiodic TTG.

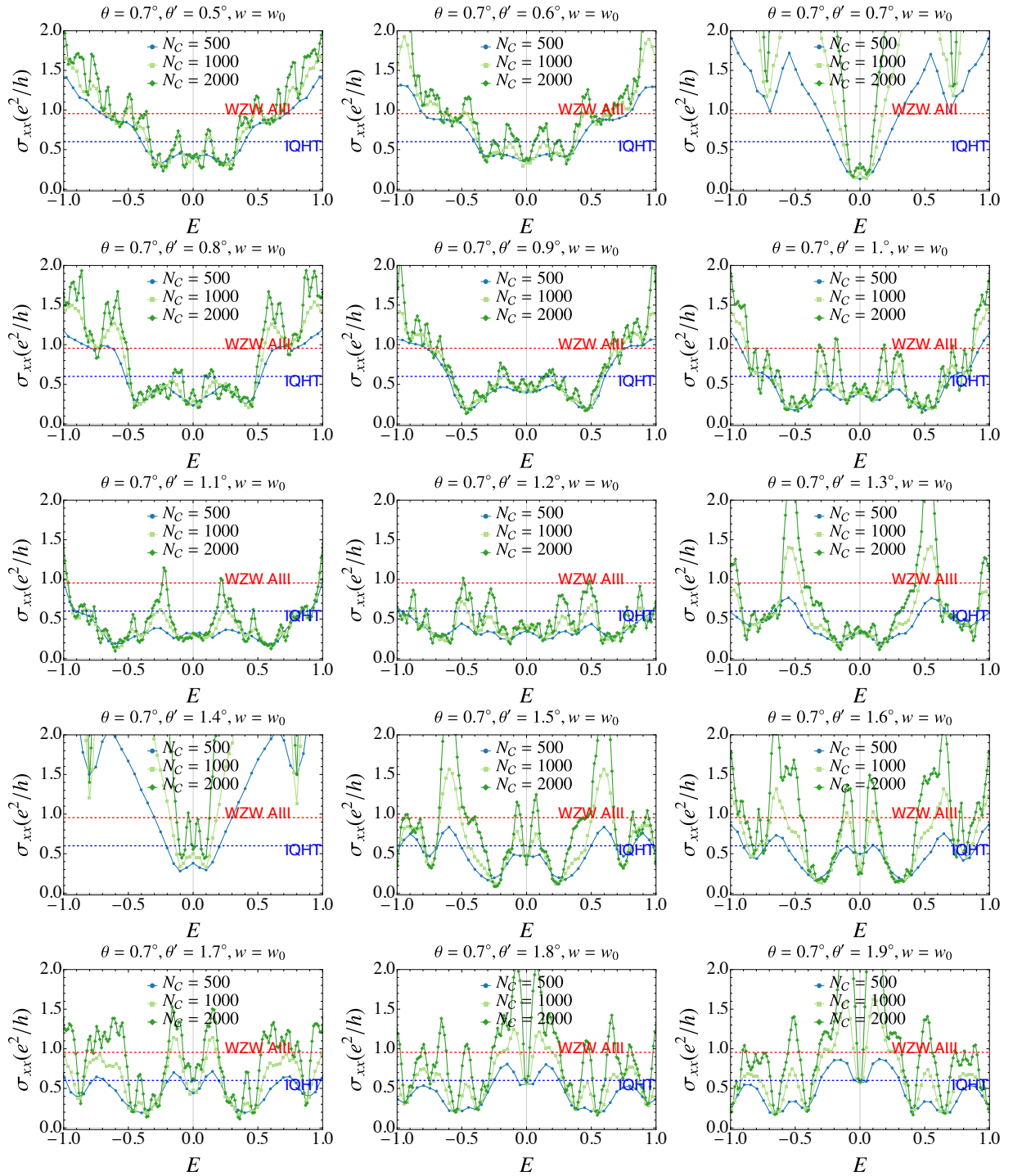


FIG. S1. The longitudinal conductivity in helical twisted trilayer graphene in chiral limit with $\theta = 0.7^\circ$, and $w = w_0$.

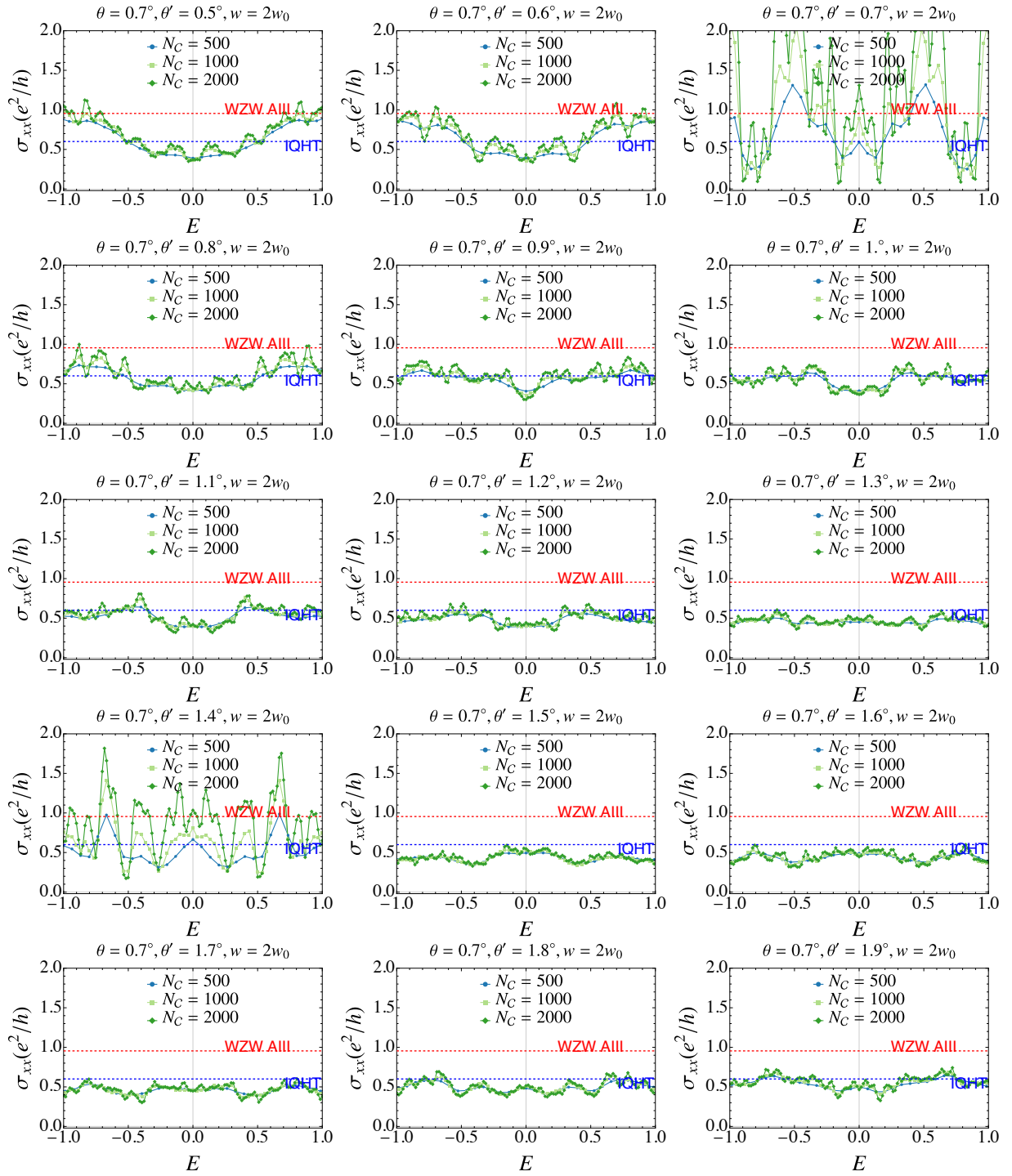


FIG. S2. The longitudinal conductivity in helical twisted trilayer graphene in chiral limit with $\theta = 0.7^\circ$, and $w = 2w_0$.

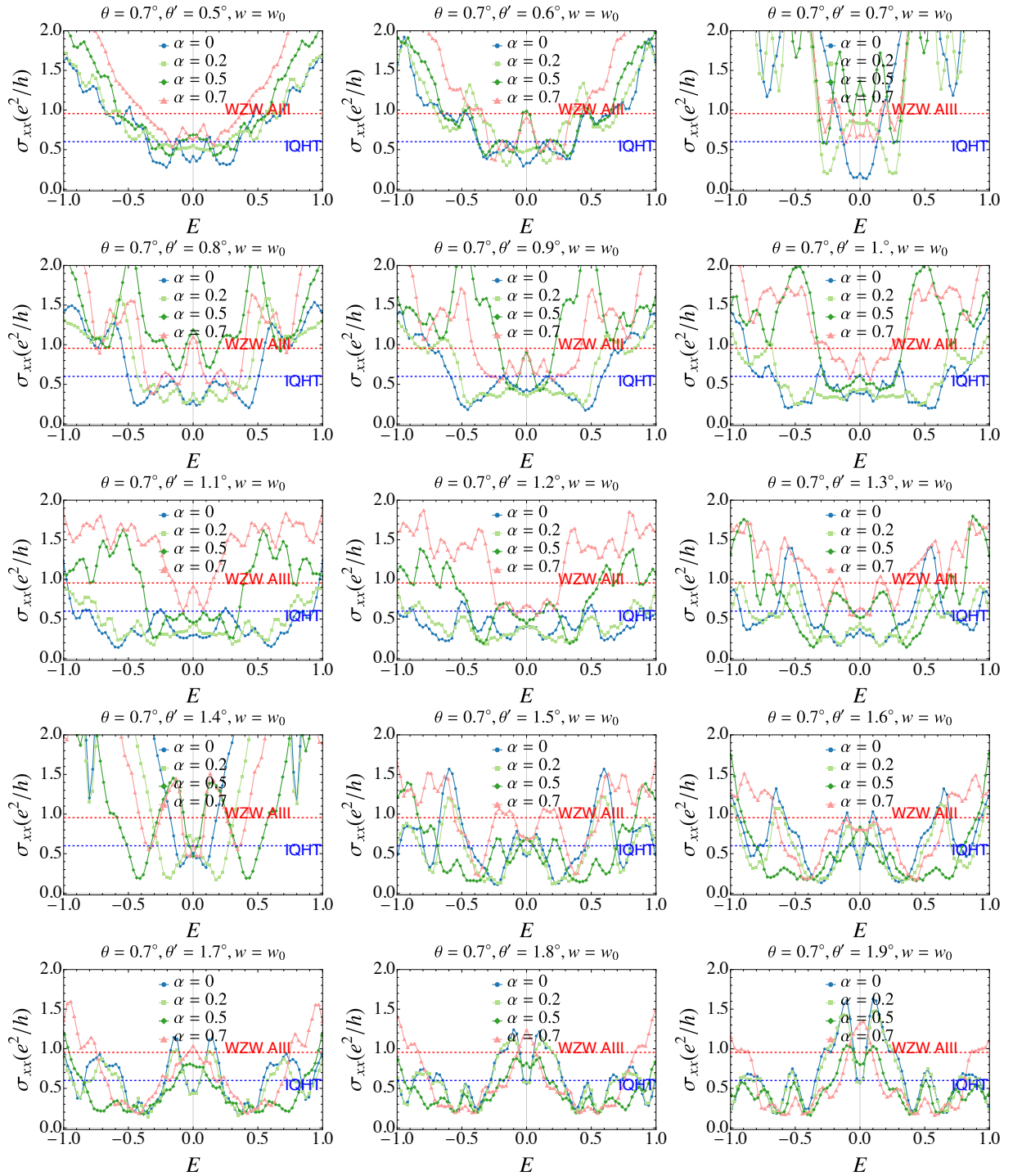


FIG. S3. The longitudinal conductivity in helical twisted trilayer graphene with chiral symmetry breaking with $\theta = 0.7^\circ$, $\alpha = 0.7$ and $w = w_0$.

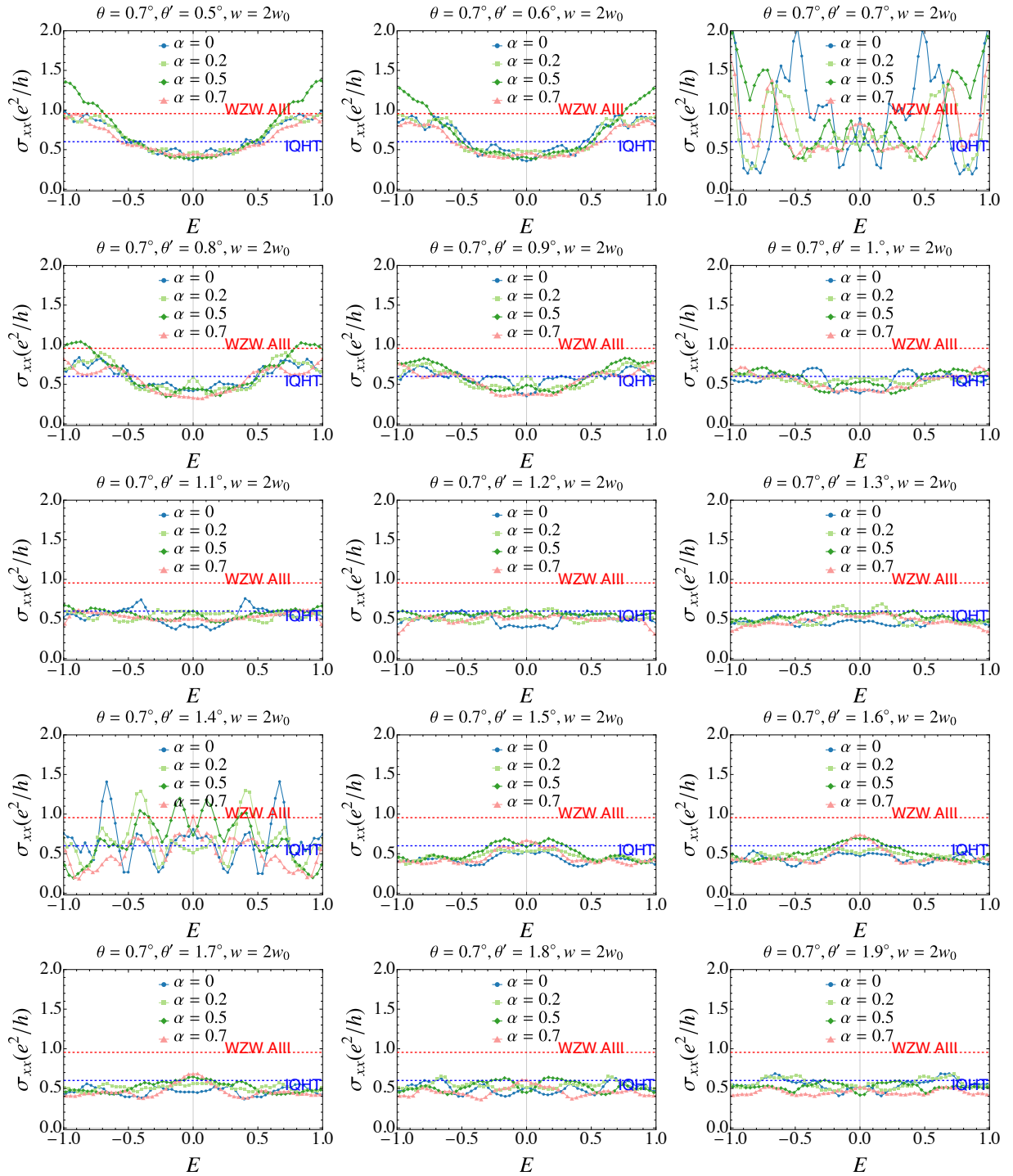


FIG. S4. The longitudinal conductivity in helical twisted trilayer graphene with chiral symmetry breaking with $\theta = 0.7^\circ$, $\alpha = 0.7$ and $w = 2w_0$.

B. Conductivity in Non-Collinear Model

Here, we test the convergence of the conductivity calculated using the non-collinear model [S3] with respect to momentum-space truncation. In the non-collinear model, interlayer tunneling couples an infinite set of momentum states generated by sums of reciprocal lattice vectors from the three rotated graphene layers. The basis states are obtained as follows:

$$\mathbf{k}^{(\ell_3)} = \mathbf{k}^{(\ell_1)} + \left(\mathbf{G}^{(\ell_2)} - \mathbf{G}^{(\ell_1)}\right) + \left(\mathbf{G}^{(\ell_3)} - \mathbf{G}^{(\ell_2)}\right), \quad (\text{S3})$$

where ℓ_1, ℓ_2, ℓ_3 denote cyclic permutations of the layer indices, and $\mathbf{G}^{(\ell)}$ ($\mathbf{G}'^{(\ell)}$) are reciprocal lattice vectors associated with layer ℓ in successive interlayer scattering processes. To truncate this infinite basis, we impose two independent cutoffs: (i) a radial cutoff G_{\max} restricting the magnitude $|\mathbf{G}^{(\ell)}|$, and (ii) a difference cutoff ΔG_{\max} restricting the momentum transfers $|\mathbf{G}^{(\ell)} - \mathbf{G}^{(\ell')}|$ generated by interlayer tunneling.

In Figs. S5 to S7, we compare the longitudinal conductivity $\sigma_{xx}(E)$ obtained using three representative choices of $(G_{\max}, \Delta G_{\max})$, both in and away from the chiral limit and for both the standard interlayer coupling $w_{AB} = w_0$ and the enhanced coupling $w_{AB} = 2w_0$. Because the non-collinear model is generically incommensurate, the momentum-space lattice of coupled states is infinite, and strict convergence with a finite cutoff is not guaranteed. Nevertheless, across all tested cutoffs the qualitative features of the conductivity remain unchanged. Away from commensurate twist-angle combinations, $\sigma_{xx}(E)$ remains approximately energy independent and of order e^2/h , while near commensurate configurations it exhibits pronounced peaks and dips, reflecting a crossover toward ballistic transport. Moreover, for the enhanced interlayer coupling $w_{AB} = 2w_0$, the conductivity is noticeably less sensitive to the choice of cutoff and remains stable across the entire energy window shown, consistent with stronger momentum mixing and critical behavior discussed in the main text.

(3, 5)

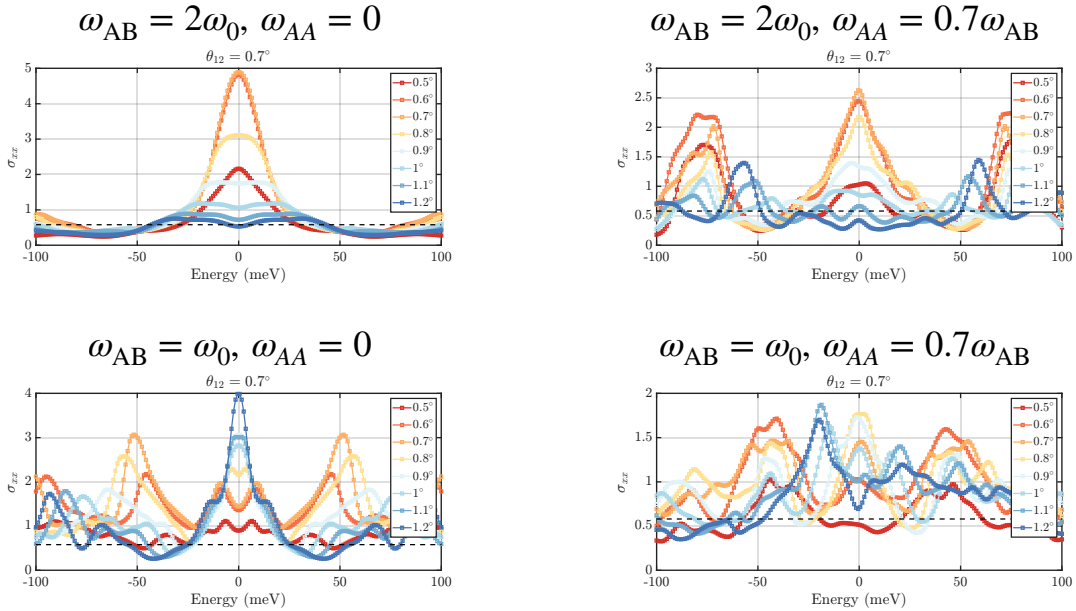
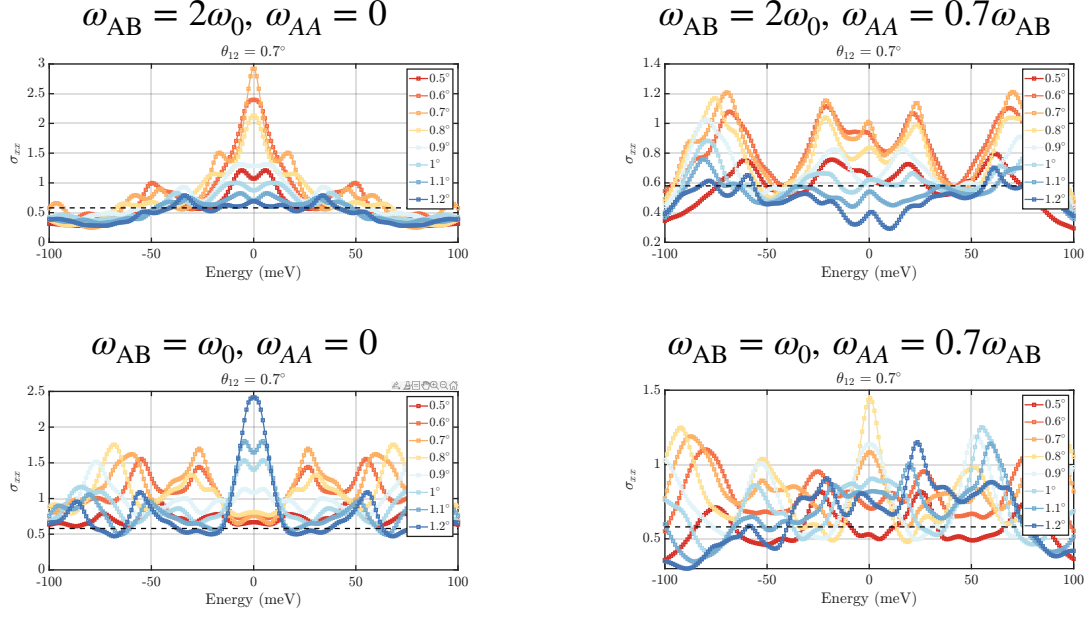
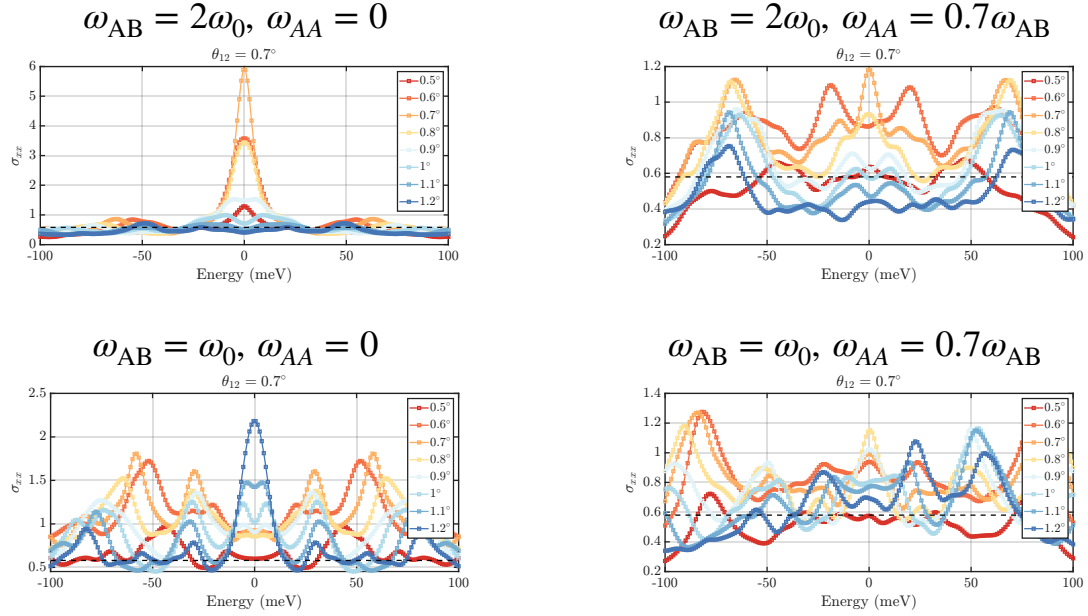


FIG. S5. Conductivity in the unit of e^2/h obtained from the non-collinear model in the chiral limit with $\theta_{12} = 0.7^\circ$ and varying θ_{23} . The smearing width is 5 meV. The black dashed line is 0.6, which is the IQHT value. Left column: with chiral limit; Right column: no chiral limit, $\omega_{AB} = 0.7\omega_{AA}$. Top row: with enhanced interlayer coupling $\omega_{AB} = 2\omega_0$; bottom row: without enhanced interlayer coupling $\omega_{AB} = \omega_0$. The cutoff radii are $|\mathbf{G}^{(\ell)}| < 3|\mathbf{G}_1|$ and $|\mathbf{G}^{(\ell)} - \mathbf{G}^{(\ell')}| < 5|\mathbf{G}_1|$ respectively.

(4, 10)

FIG. S6. Same as Fig. S5, with cutoff radii $|\mathbf{G}^{(\ell)}| < 4|\mathbf{G}_1|$ and $|\mathbf{G}^{(\ell)} - \mathbf{G}^{(\ell')}| < 10|\mathbf{G}_1|$.

(6, 10)

FIG. S7. Same as Fig. S5, with cutoff radii $|\mathbf{G}^{(\ell)}| < 6|\mathbf{G}_1|$ and $|\mathbf{G}^{(\ell)} - \mathbf{G}^{(\ell')}| < 10|\mathbf{G}_1|$.

III. DENSITY OF STATES IN HELICAL TWISTED TRILAYER GRAPHENE

Figs. S8 and S9 show the density of states (DOS) of helical twisted trilayer graphene at ambient pressure in the chiral limit and with chiral symmetry breaking, respectively. At commensurate twist angles, a pronounced zero-energy peak appears in the chiral limit, corresponding to flat bands. When chiral symmetry is broken, these flat bands disappear and the DOS recovers the linear energy dependence characteristic of Dirac fermions. At incommensurate

angles, the DOS exhibits a highly spiky structure across energy, reminiscent of the Aubry–André model, reflecting the quasiperiodic nature of twisted trilayer graphene.

Figs. S10 and S11 show the DOS at higher pressure ($w = 2w_0$). Compared with ambient pressure, the DOS is significantly smoother, consistent with the enhancement of quantum criticality at enhanced pressure.

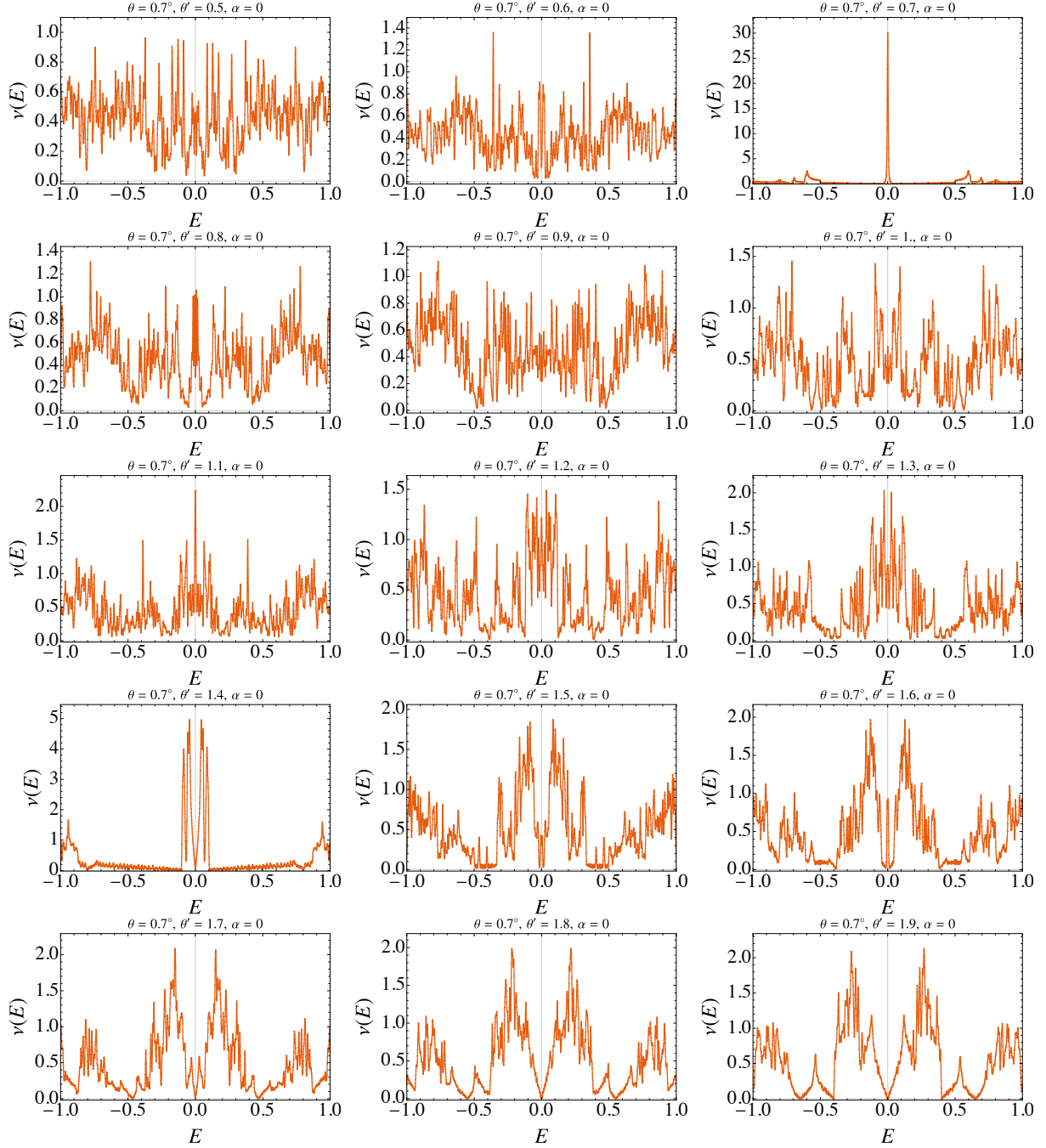


FIG. S8. The DOS in helical twisted trilayer graphene at ambient pressure ($w = w_0$) and in the chiral limit ($\alpha = 0$).

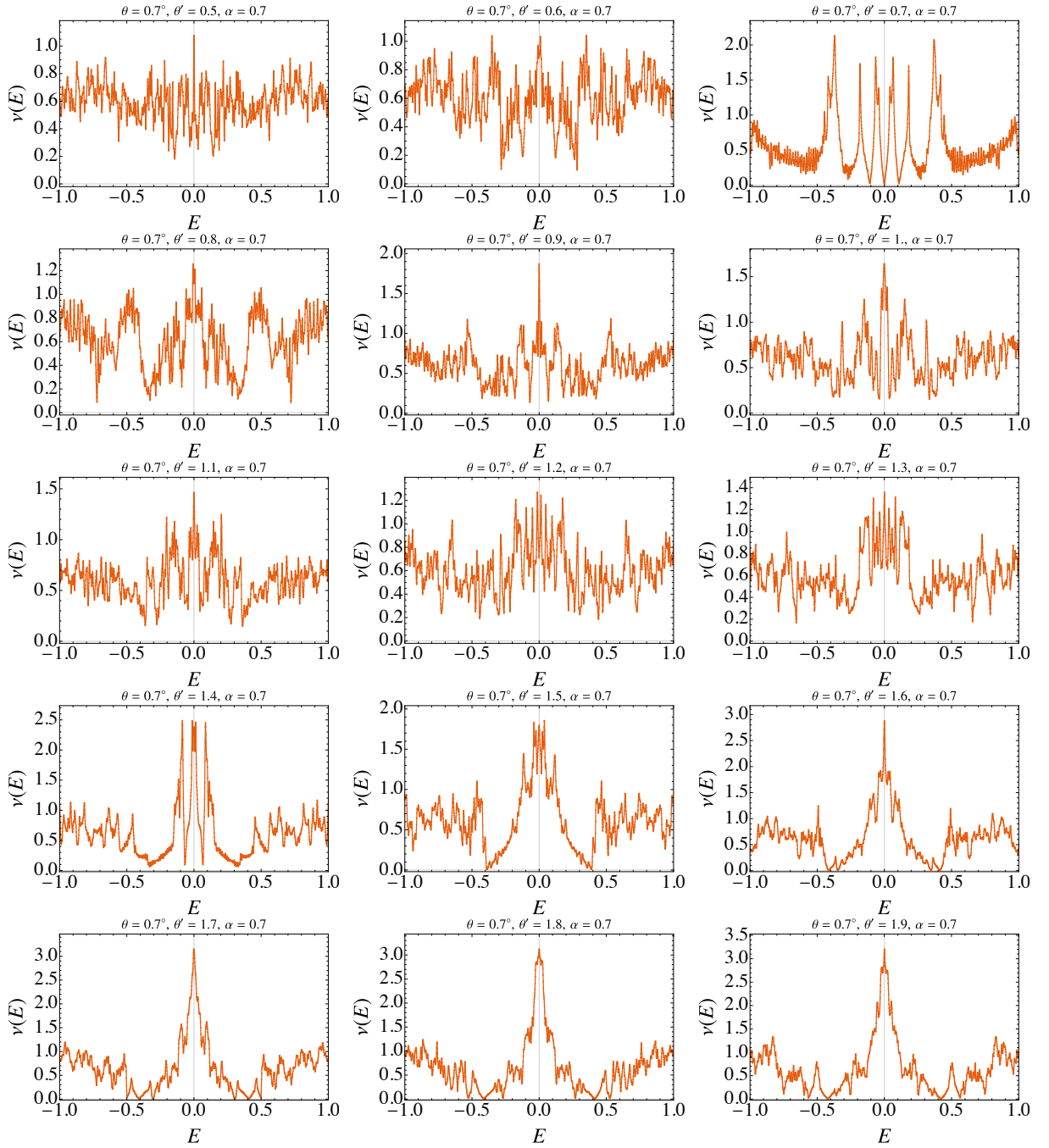


FIG. S9. The DOS in helical twisted trilayer graphene at ambient pressure ($w = w_0$) with chiral symmetry breaking ($\alpha = 0.7$).

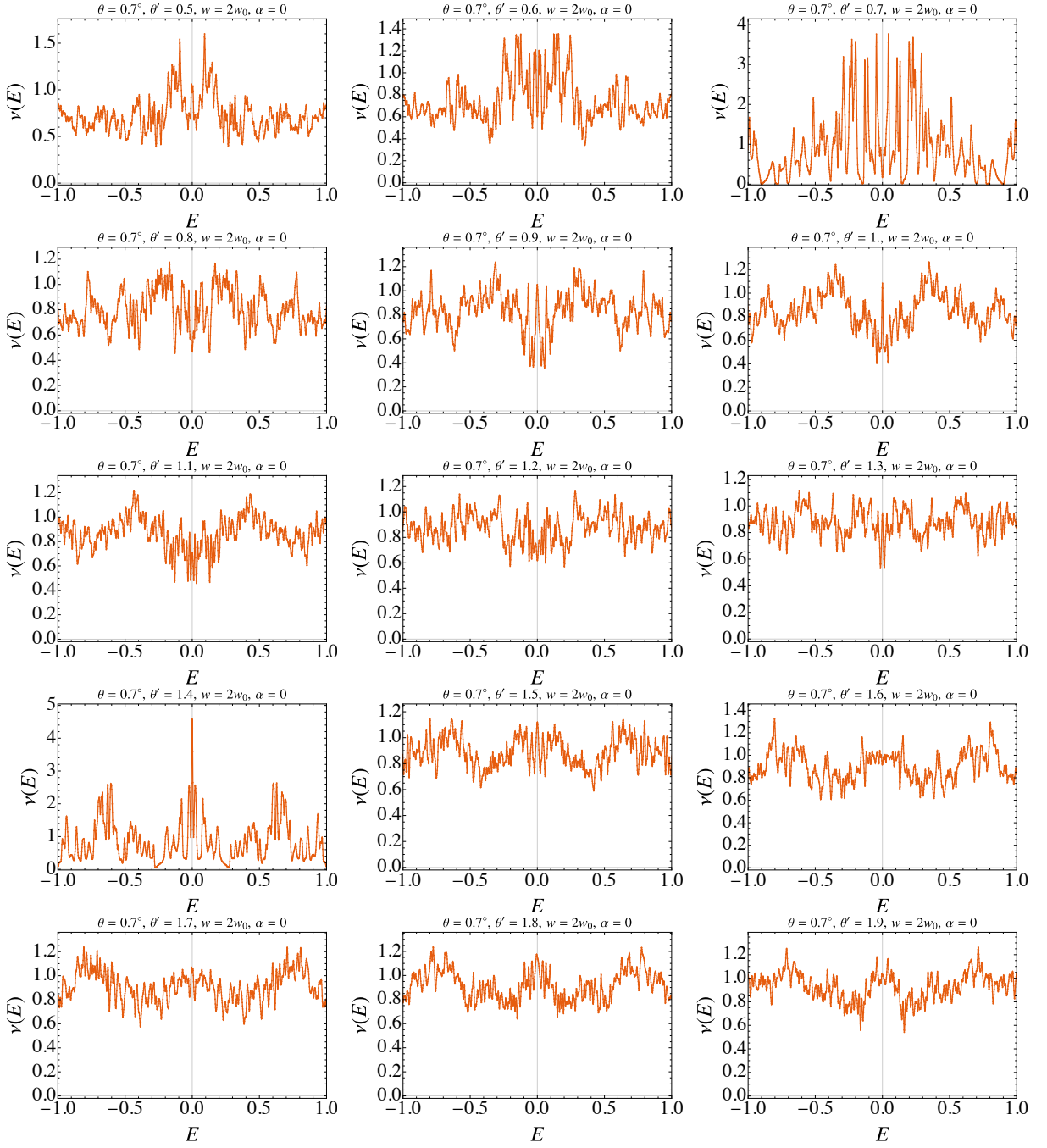


FIG. S10. The DOS in helical twisted trilayer graphene in the chiral limit ($\alpha = 0$) and at high pressure ($w = 2w_0$).

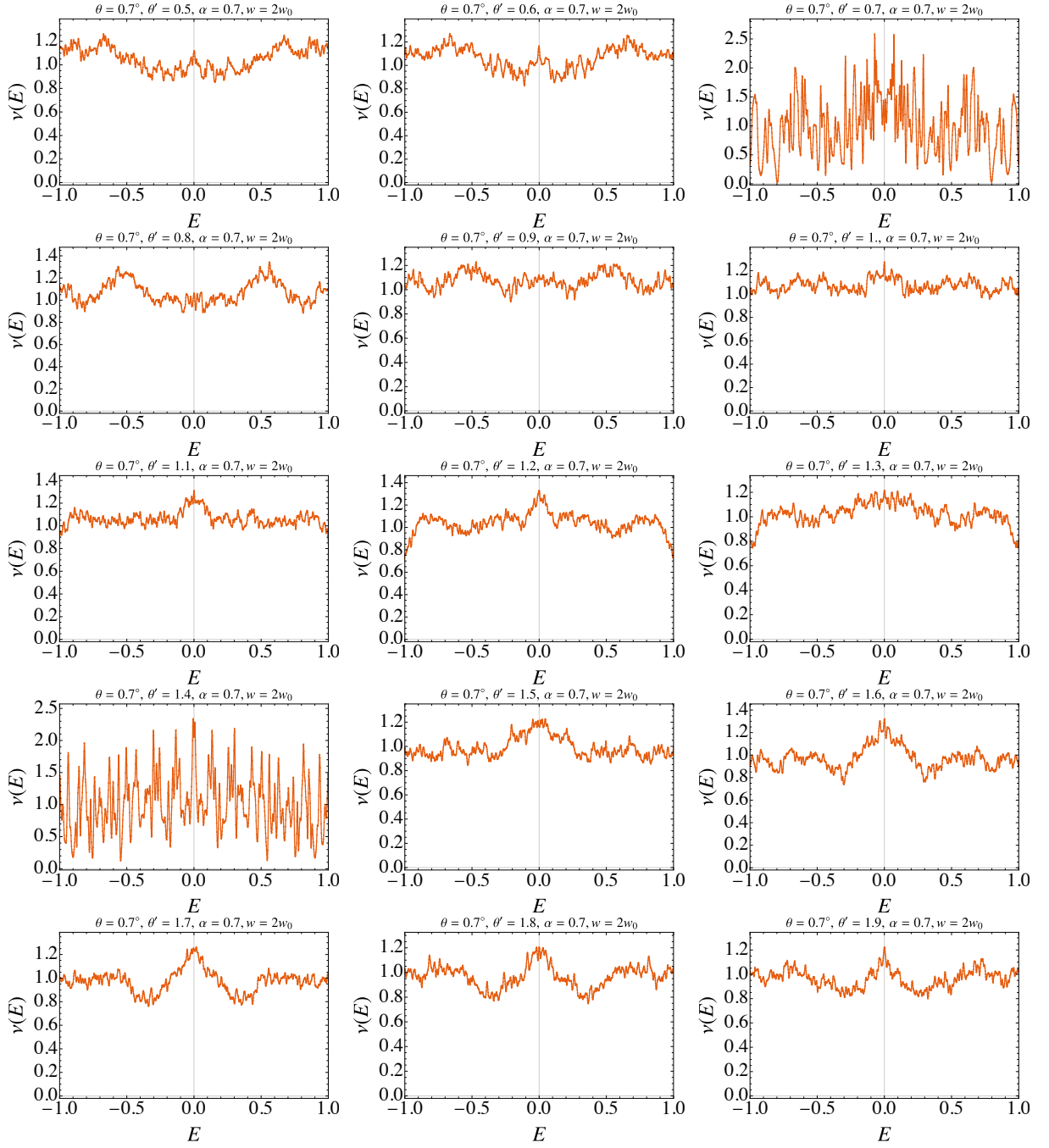


FIG. S11. The DOS in helical twisted trilayer graphene with chiral symmetry breaking term ($\alpha = 0.7$) and at high pressure ($w = 2w_0$).

-
- [S1] Weiße, A., Wellein, G., Alvermann, A. & Fehske, H. The kernel polynomial method. *Rev. Mod. Phys.* **78**, 275–306 (2006). URL <https://link.aps.org/doi/10.1103/RevModPhys.78.275>.
- [S2] Zhang, X., Wilson, J. H. & Foster, M. S. Critical filaments and superconductivity in quasiperiodic twisted bilayer graphene. *Phys. Rev. B* **111**, 024207 (2025). URL <https://link.aps.org/doi/10.1103/PhysRevB.111.024207>.
- [S3] Zhu, Z., Carr, S., Massatt, D., Luskin, M. & Kaxiras, E. Twisted Trilayer Graphene: A Precisely Tunable Platform for Correlated Electrons. *Phys. Rev. Lett.* **125**, 116404 (2020). URL <https://link.aps.org/doi/10.1103/PhysRevLett.125.116404>.